Vector Boson Fusion Topology and Simplified Models for Dark Matter Searches at Colliders

Submitted in fulfilment of the requirements
for a degree of Master in Science

presented by

Daniel Ocampo Henao

and supervised by

José David Ruiz Álvarez

Medellín
2023

Abstract

We study possible searches of Dark Matter at colliders using Vector Boson Fusion topology under the context of Simplified Models signatures. We examine the experimental sensitivity to probe these signatures with respect to monojet-type searches, and determine how these two scenarios might be complementary.

Keywords: dark matter, simplified models, colliders.

Resumen

Estudiamos las posibles búsquedas de materia oscura en colisionadores utilizando la topología VBF (*Vector Boson Fusion*) en el contexto de señales de modelos simplificados. Examinamos el posible alcance de estas búsquedas con respecto a las búsquedas de tipo *mono-jet*, y determinamos cómo estas dos señales podrían ser complementarias.

Keywords: materia oscura, modelos simplificados, colisionadores.

Contents

List of Figures

List of Tables

Introduction

The particle nature of dark matter is one of the most intriguing questions in particle physics today. It has been theorized to be responsible for one quarter of the total energy content of the universe. This fraction is usually referred to as dark matter (DM). We have several sources of evidence pointing to the existence of this unknown form of matter from different types of astronomical measurements [11, 12, 13, 14]. However, direct and indirect searches have failed to find a particle which could explain the dark matter abundance.

The quest towards dark matter discovery can be also pursued in particle colliders as the Large Hadron Collider (LHC). Several searches have been conducted by the ATLAS and CMS experiments at the LHC [15, 16, 17, 18, 19, 20], without positive indication of the production of a DM particle.

Several theoretical frameworks have been developed to explore DM searches at colliders. For example, simplified models [21, 2] provide useful benchmark scenarios to probe the production of DM at the LHC that have been introduced in recent years. These models provide a rather free theoretical approach and simple interpretation framework. Therefore, it is interesting to envisage all possible signatures for DM searches within this approach.

We study the production of DM at the LHC through the Vector Boson Fusion (VBF) topology, considering different simplified model scenarios. The corresponding event selection criteria is optimized for best signal significance in order to maximize the experimental sensitivity. Our findings are compared to monojet-type searches and show VBF signatures complementarity for DM searches.

The thesis is organized as follows: In Chapter 1 a brief overview of the standard model of particle physics is provided, giving special attention to the strong and electroweak interactions. Dark matter evidence, search strategies and simplified models are described in this chapter. The experimental setup of the LHC accelerator and the Compact Muon Solenoid experiment are detailed in Chapter 2. A description of the reconstruction of the collision events collected by the CMS detector is provided. Also, the reconstruction algorithms of the relevant final state objects, such as jets and MET, are discussed. Chapter 3 presents an overview of the simplified models used, emphasizing relevant aspects of the VBF topology. Section 3.2 introduces the simulation models, software and techniques exploited for the simulation of proton-proton (pp) collisions used in this work. The further event selection and the respective selection criteria is described in section 3.3. The conclusions of the work are presented in Chapter 4.

Chapter 1

Theoretical framework

This chapter discusses the Standard Model of particle physics (SM) and the motivation for extending the SM with a theory that has a Dark Matter candidate. It starts with an overview of the SM, briefly summarizing the electroweak and strong interactions. Additionally, it motivates the search for DM and introduces the different types of DM searches, with a particular focus on collider searches. Finally, it introduces the simplified model used for this analysis.

1.1 The standard model of particle physics

The SM describes the basic constituents of matter and the fundamental interactions among elementary particles. Over the past 50 years it has been tested by numerous experiments and has been shown to provide an accurate description of particle interactions at different energy scales. The SM incorporates two fundamental theories, the theory of electroweak interactions and quantum chromodynamics (QCD). The SM Lagrangian can be written as a sum of three terms, one related to QCD, one to the electroweak interaction, and one to the Higgs field:

$$L_{SM} = L_{QCD} + L_{EW} + L_{\text{Higgs}} \tag{1.1}$$

Electroweak theory, also known as Glashow-Weinberg-Salam theory, is a unified theory describing the weak and electromagnetic interactions of elementary particles. Glashow began in 1961 [22] combining the electromagnetic and weak forces using the SU(2) $\times$ U(1) symmetry group. He was followed in 1967 by Salam and Weinberg [23, 24], who used the Higgs mechanism [25, 26] to continue building the formalism. The Higgs mechanism allowed both gauge bosons and fermions to acquire mass without breaking gauge invariance. However, the theory was not properly promoted until Gerard 't Hooft showed that it was self-consistent and renormalizable [27, 28]. QCD is described by the SU(3) symmetry group, which represents the color symmetry. The concept originated from the idea that the threefold color charge is the cause of the strong interaction among quarks [29, 30]. This principle was adopted as the theory of the strong interaction after the discovery of asymptotic freedom [31, 32].

Figure 1.1 shows a summary of the SM: names, masses, spins, and charges of the Higgs boson, quarks and leptons, and gauge bosons. The building blocks of matter are spin-1/2 fermions, the three generations of quarks and leptons. The interaction among these fermions occurs through the exchange of spin-1 particles. The electromagnetic

interactions are mediated by photons (γ), the weak interactions are mediated by the $W^{\pm}$ and Z bosons, and the strong interactions are mediated by gluons (g). These mediators are called gauge bosons because they arise from local gauge symmetry invariance. The Higgs boson in the SM arises from spontaneous symmetry breaking, which allows the $W^{\pm}$ and Z bosons to acquire mass without breaking gauge invariance.

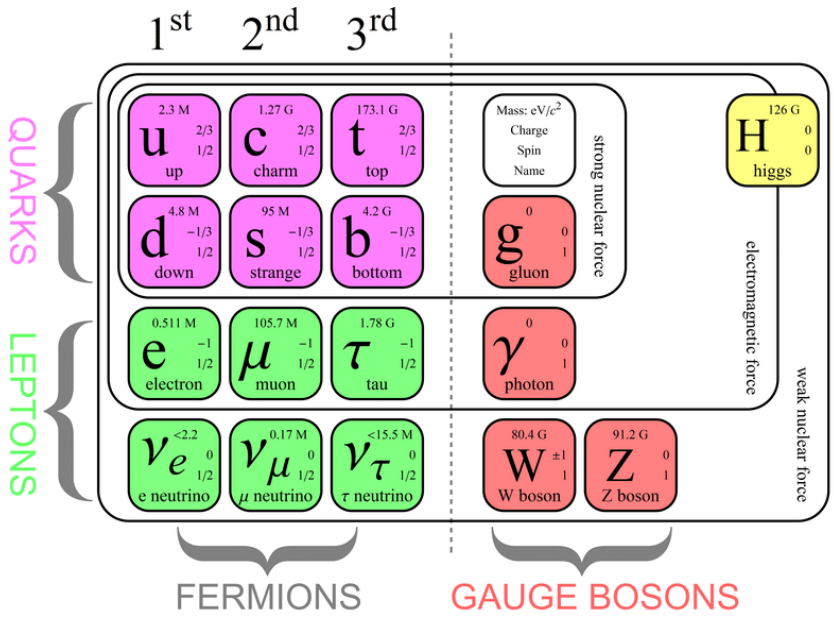

Figure 1.1: Particle content of the Standard Model [1].

1.1.1 Strong interactions

As explained above, QCD describes strong interactions among particles with color charge: six quarks and eight linearly independent color gluon states, corresponding to "eight kinds" or "eight colors" of gluons. While quarks (anti-quarks) have a color (anti-color), gluons themselves have a color and an anti-color charge at the same time. The combination of one color and its corresponding anti-color, as well as the combination of all colors or all anti-colors, results in a "colorless" state. Gluons bind to quarks of the same flavor and different colors, and as a consequence of the SU(3) symmetry group, trilinear and quartic self-interaction vertices are possible for gluons.

The strength of the strong interaction is described by the strong coupling constant α_s, which depends on the energy scale Q. The value of α_s increases rapidly with decreasing Q, meaning that the interaction among quarks becomes stronger the further apart they are in distance. This property is referred to as *color confinement* and explains why gluons and quarks, collectively referred to as *partons*, have never been observed as bare states. One might think that with enough energy, it should be possible to separate quarks from their bound states, but when the gluon field reaches a critical energy quark-anti-quark pairs emerge from the vacuum. The two colored objects cannot be separated from each other and appear in a synthesized neutral color state called *hadrons*. Experimentally, after hadronic collisions, the partons produced fly away from the interaction point. Because of the traveling nature of the strong coupling constant, the interaction strength between the traveling partons increases as they move away, and quark-quark pairs are produced. Furthermore, the partons produced recombine with each other to form neutral colored objects, creating a group of hadrons moving in a collimated direction. This process is

called *hadronization*.

Hadrons are classified by their valence quarks, which determine the quantum numbers of hadrons. However, the structure of hadrons also includes virtual quarks and gluons, since quarks can interact via gluons creating virtual quark-anti-quark pairs. These virtual quarks and gluons do not contribute to the quantum numbers of hadrons. Particles such as protons and neutrons are classified as baryons, which are hadrons composed of an odd number of valence quarks. A meson is a hadron composed of a quark-anti-quark valence pairs. Protons are the only known stable baryons, while mesons are all unstable.

Another important feature of the strong coupling constant is that it decreases with increasing Q, which means that the coupling becomes weaker at high energies (equivalent to short-distance interactions). This behavior is called *asymptotic freedom*, which allow us to think of quarks in this region as if they were free particles, so we can describe their interactions approximately by means of a perturbative expansion in terms of α_s. The accuracy of a perturbative QCD calculation with the minimum order of α_s is the so-called leading order (LO) accuracy. Similarly, the next-to-leading order (NLO) accuracy is the calculation that includes an additional contribution of the second lowest order of α_s.

1.1.2 Electroweak interactions

The electromagnetic interaction is described by the Quantum electrodynamics theory (QED). Electromagnetic interactions among charged fermions are mediated by photons, which are massless vector bosons with no charge. Since the strength of the electromagnetic interaction ($\alpha_{em} \approx 1/137$) is considerably smaller than one, the QED process can be accurately described using perturbative expansions. Charged weak interactions are associated with $W^{\pm}$ bosons, while Z bosons mediate neutral weak interactions, coupling with fermions and antif-ermions of the same flavor. The weak interaction is the only one of the fundamental forces that involves all fermions, and it name arises from the fact that its strength is many orders of magnitude smaller than that of the electromagnetic force and the strong interaction.

Weak and electromagnetic interactions are unified into the electroweak theory, which is described by the $\mathrm{SU}(2)_L \times \mathrm{U}(1)_Y$ symmetry group [33]. Although this model predicts massless $W^{\pm}$ and Z bosons, the masses of these particles were experimentally measured with very good accuracy to be 80.4 GeV and 91.2 GeV, respectively [34]. To explain the non-zero mass of the $W^{\pm}$ and Z bosons, the SM was extended by adding a scalar quantum field (Higgs field) which, by means of a spontaneous breaking of the electroweak symmetry, gives mass to the particles with which it interacts [26]. The interaction between the Higgs field and fermions is described by a Yukawa coupling that introduces a mass term proportional to each fermion's unique Yukawa coupling constant y_f [33].

1.2 Dark Matter

It is approximately 90 years since Fritz Zwicky published the first scientific paper discussing the idea of DM, a type of non-luminous matter that interacts gravitationally with ordinary matter [35]. Since then, substantial evidence for the presence of DM has emerged (mainly gravitational evidence on astrophysical scales).

The cosmic microwave background (CMB) is microwave radiation that fills all space [36], and its measurement is without a doubt one of the most compelling proofs of the

existence of DM in our universe. Its spectrum allows for a thorough examination of the ΛCDM model, a cosmological model with a dark component in the form of DM and dark energy [37]. This model is quite successful in accurately accounting for the vast majority of current cosmological observations [38]. Planck observations of the CMB have reached sub-percent accuracy, with precision of the order of one percent for the ΛCDM parameters. These accurate measurements imply that the matter energy budget of the cosmos has a non-negligible DM component of the order of 85% and roughly 25% of its overall energy density [39].

The SM fails to answer a number of crucial points. In particular, it is unable to explain the presence of DM [40]. Many hypotheses have been proposed [41]. One plausible explanation is that there are new elementary particles that can explain the DM relic abundance, whose evolution has followed a similar path to the SM particle content evolution [42]. Since DM interacts weakly with SM particles, it can be assumed to have formed from the release of weakly interacting massive particles (WIMPs) that were in thermal equilibrium with SM particles at some point in the early universe. These WIMPs can be searched in multiple ways. In the direct detection approach, one searches for the scattering of a DM particle and a particle from the standard model (LUX [43], DARKSIDE [44], Xenon [45]). Another strategy is to look for DM production at colliders, particularly at the Large Hadron Collider (LHC) [46].

1.2.1 Simplified models

Within the scope of performing searches for DM at the LHC, a DM theory is required to interpret the results. Many different approaches have been proposed, each of which contains particles that are viable candidates for DM. These theories cover the theoretical space of all non-SM physical realizations.

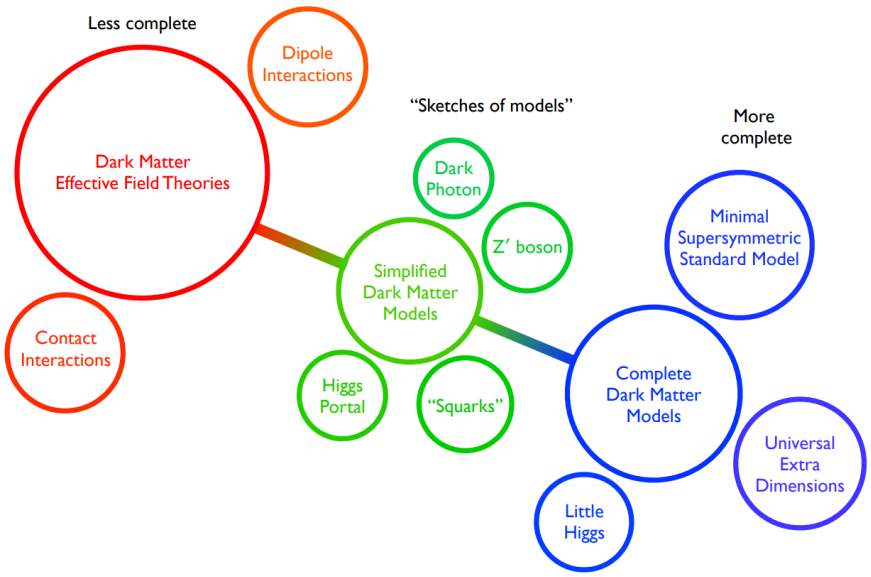

Figure 1.2: Dark Matter theory space [2].

Possibly, the first approach considered has been the neutralino candidate within a Minimal Supersymmetric Standard Model (MSSM) theoretical framework [47, 48]. However it has been quickly identified that this approach has liminations and strong theoretical constrains. More generic models have been proposed as the Inert Dark Matter model [49, 50].

These models have theoretical constrains as well, which limit the available phase-space to be probed at the LHC.

Finally, the last step before the arrival of simplified models has been the effective field theory (EFT) approach [51, 52]. In this theory, the mediator that communicates the DM candidate with the SM is very heavy, and thus escaping the energy reach of the LHC. This has strong implications for the kinematic properties of the DM production signatures, making it extremely difficult to search for a DM candidate with a rather light mediator.

At this point, the simplified models were proposed as an intermediate solution among the EFT and complete models. Simplified models allow having a quite complete theoretical picture with a very unrestricted modelling and an easy framework for reinterpretations. Therefore, these models can be used to inspire and design searches at the LHC, but can also be used to interpret LHC results and analyze them into the context of complete models, as the MSSM.

Chapter 2

Compact Muon Solenoid Experiment

2.1 The Large Hadron Collider

The Large Hadron Collider (LHC) [46] is the most ambitious experiment on earth. It is a powerful circular particle accelerator, located on the border between Switzerland and France in a pre-existing 27 km long tunnel. It is designed to accelerate and collide proton beams (or heavy ions). These beams are initially accelerated through smaller accelerators until they eventually get to the main ring, where they reach their maximum velocity using a system of superconducting magnets. These proton bunches collide approximately every 25 ns at four interaction points, where the CMS [53], ALICE [54], ATLAS [55] and LHCb [56] experiments are located. A schematic representation of the CERN accelerator complex is given in Figure 2.1.

2.1.1 Luminosity

Luminosity $\mathcal{L}$ is a key property for a particle collider such as the LHC. It is associated to the number of protons per area per unit time: for two colliding bunches with N_1 and N_2 numbers of particles, the luminosity can be expressed as:

$$\mathcal{L} = \frac{N_1 N_2 f n_b}{A_{eff}}\,, \tag{2.1}$$

where n_b is the number of colliding bunches and f the frequency in the collider. These values, together with N_1 and N_2, are obtained from measurements of the LHC machine [57, 58, 59]. The luminous region parameter A_{eff} is related to the effective area of the colliding bunches or beam overlap area [60]. The integrated luminosity $L = \int \mathcal{L}\ dt$, is related to the cross-section σ and the total number of events through the relation $N_{events} = \sigma \cdot L$.

The luminosity plays a central role in the machine diagnostics and optimization. Figure 2.2 shows the integrated luminosity of proton-proton collisions for different data taking periods and energies at the CMS experiment.

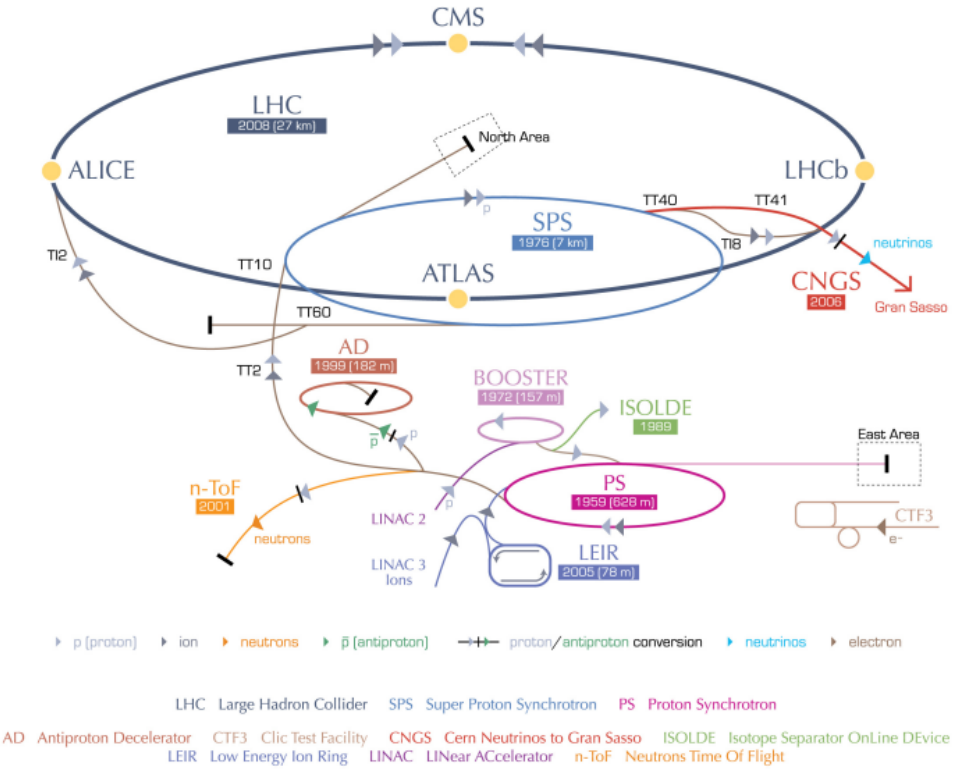

Figure 2.1: The accelerator complex at the CERN laboratory [3]

2.2 The CMS Experiment

The Compact Muon Solenoid (CMS) detector is located at one of the interaction points of the LHC ring (see Figure 2.1). It is a cylinder along the beam axis, where the different sub-detectors are arranged like concentric layers, with encap disks perpendicular to the beam pipe as shown in Figure 2.3.

Its design is very efficient in collecting information near the interaction point, necessary to distinguish between particles originating at the interaction point (primary vertex) and those coming from subsequent decays (secondary vertices). As its name indicates, it also allows to reconstruct with great precision muons generated in the collisions.

The main components of the detector can be divided into a silicon tracker, an electromagnetic calorimeter (ECAL), a hadron calorimeter (HCAL), a superconducting solenoid, and the muon chambers, as shown in Figure 2.4.

2.2.1 Coordinate system

The coordinate system use by the CMS experiment is shown in Figure 2.5. The z-axis is chosen alongside the beam line, the x-axis points directly to the center of the LHC ring and the y-axis upwards. The azimuthal angle ϕ is defined from the positive x-axis in the (x, y) plane (transverse plane), while the polar angle θ is measured from the positive z-axis.

For a given particle the rapidity y and pseudo rapidity η are defined as:

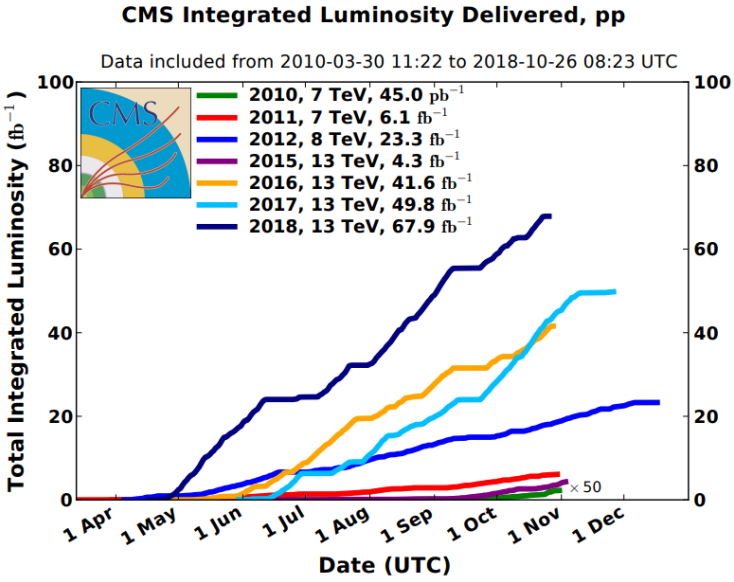

Figure 2.2: Integrated luminosity of proton-proton collisions for different data-taking periods at $\sqrt{s} = 7$, 8, and 13 TeV. Taken from [4].

$$y = \frac{1}{2} \ln \left(\frac{E + p_z}{E - p_z} \right), \tag{2.2}$$

$$\eta = -\ln \left[\tan \left(\frac{\theta}{2} \right) \right], \tag{2.3}$$

where E and p_z are the energy and the z projection of the momentum vector $\mathbf{p}$, respectively. These observables are very useful since the difference in rapidities or pseudorapidities between two particles is invariant with respect to a Lorentz boost along the beam axis.

The coordinates to describe outgoing particles in the detector are (ϕ, η, p_T), where p_T is the projection of the momentum vector in the transverse plane.

2.2.2 Tracking system

The tracking system is the innermost part of the detector, made of segmented silicon pixel and silicon strip detectors (Figure 2.6). The silicon pixel detector consists of four barrel layers and two endcaps of pixel modules per side. The innermost layer and the endcaps are placed close to the interaction point in order to have a high precision in the interaction vertices reconstruction [61, 62]. The silicon strip tracker consists of inner and outer barrels with four and six concentric layers respectively, three tracker inner disks on each side, and a tracker endcap which extends the coverage up to $|\eta| = 2.5$ with nine disks on each side [7].

The tracking system is immersed in a 3.8 T magnetic field generated by the superconducting solenoid. This configuration allows to reconstruct the curve trajectories (tracks) of the charged particles. These tracks are used for the determination of the momenta and charge sign of the particles.

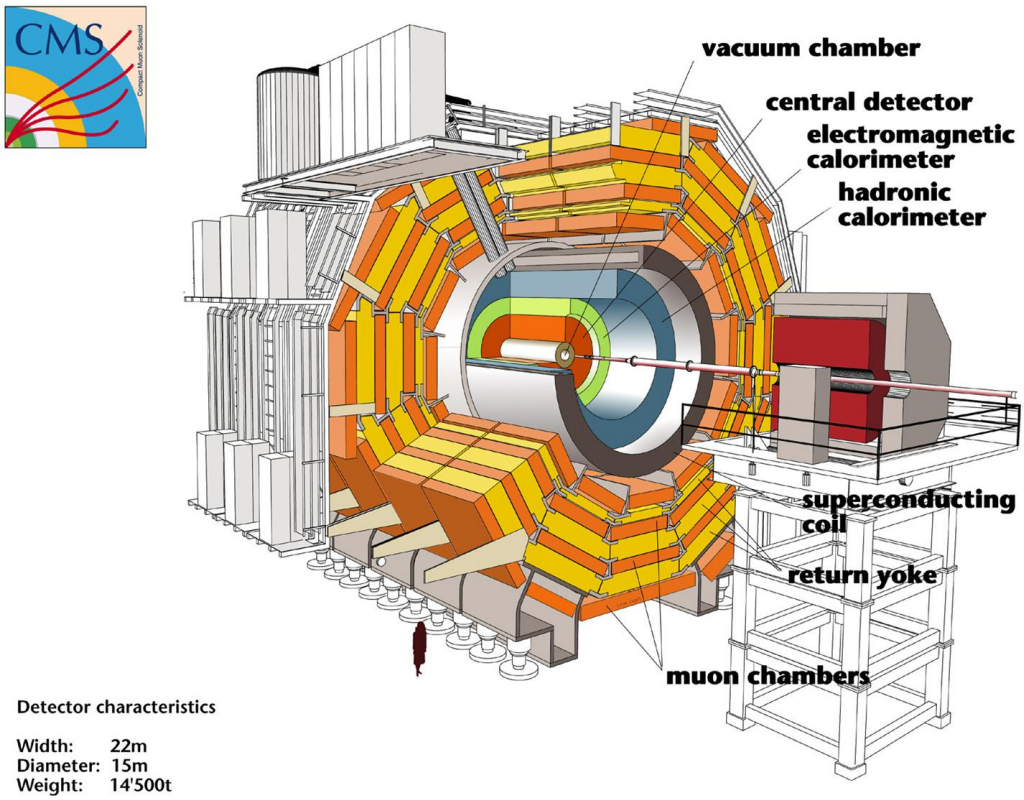

Figure 2.3: Overview of the CMS components. (Credits: CERN)

2.2.3 Calorimeters

The main purpose of a calorimeter is the measurement of a particle's energy. This is achieved by stopping the neutral and charged particles in a high density material. The CMS detector has two calorimeters:

- **The electromagnetic calorimeter** (ECAL): is an homogeneous and fine-grained calorimeter, made of lead tungstate crystals surrounding the tracker system. Its design (Figure 2.7), allows to retain most of the energy deposited by electrons and photons [63, 64]. The barrel section and the endcap modules covers the $|\eta| < 1.479$ and $1.479 < |\eta| < 3.0$ ranges, respectively. The endcap modules. With the goal of enhancing the electromagnetic shower, a preshower detector is placed before the endcap crystals in the range $1.653 < |\eta| < 2.6$.

- **The hadronic calorimeter** (HCAL): It is located between the ECAL and the solenoid. It is composed of brass radiators and scintillator sensors. The barrel (HB) and the endcap (HE) covers the $|\eta| < 1.3$ and $1.3 < |\eta| < 3.0$ ranges, respectively. These are complemented with an outer calorimeter (HO) in the range $0 < |\eta| < 1.26$, located in front of the muon chambers just inside the steel yoke. The pseudorapidity range is further extended up to $|\eta| = 5.2$ with the forward hadron calorimeter (HF) located surrounding the beamline, as shown in Figure 2.8 [8]. The HCAL measures the energy deposited by strongly-interacting particles, which are essential for jets detection and the determination of p_T^{miss} [8].

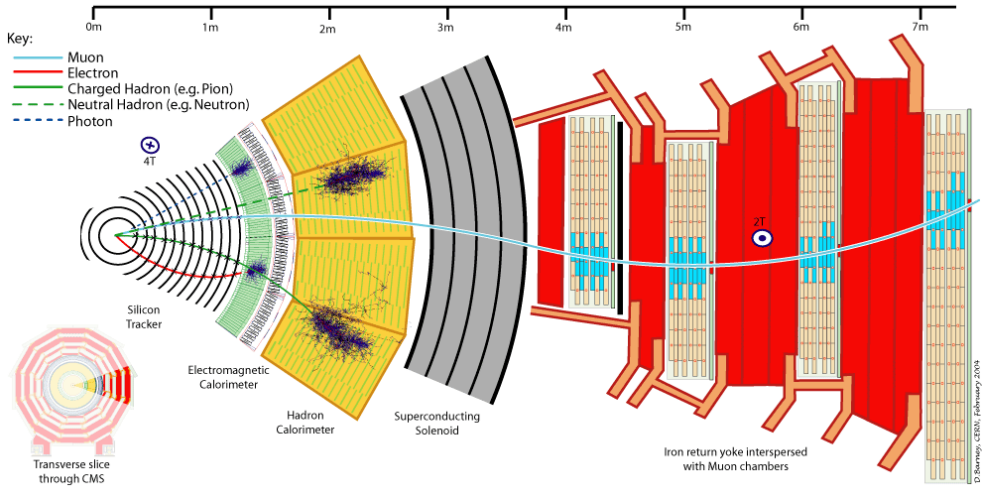

Figure 2.4: A sketch of the specific particle interactions in a transverse slice of the CMS detector, from the beam interaction region to the muon detector [5].

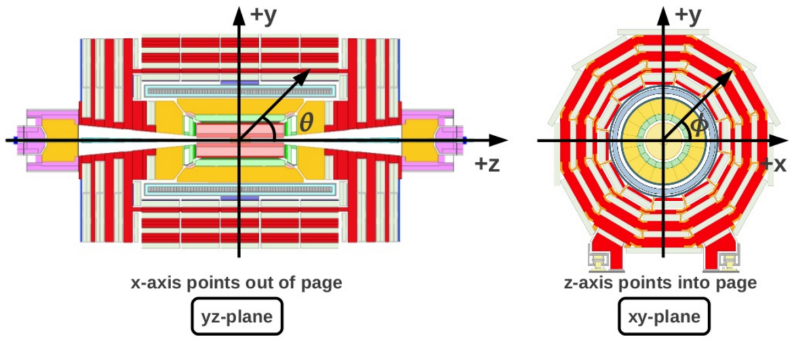

Figure 2.5: Coordinates system used in the CMS experiment [6].

2.2.4 Muon Chambers

This system is formed of three kinds of gaseous detectors, designed to detect muons and measure their trajectories in a very optimized fashion. It has a spatial resolution around 100 μm and, together with the information from the tracker, it achieves a momentum resolution of 1% - 3% for 20 GeV $\lesssim p_T^{\text{muon}} \lesssim$ 100 GeV [9]. As shown in Figure 2.4, the system parts are intercalated with the flux-return yokes covering the $|\eta| < 2.4$ region.

2.3 Object reconstruction

The physics object reconstruction in CMS is accomplished using an algorithm called Particle Flow (PF) [5]. It uses the whole information gathered by the subdetectors to reconstruct energy, momentum and trajectory of each stable particle. First, the PF algorithm identifies the quantities measured by each subdetector, such as tracks from electrically charged particles, measured in the silicon tracker, energy clusters in calorimeters or muon tracks in the outer section of the detector. The algorithm groups these signatures into blocks according to whether they could be associated to the same particle. As an example, a charged particle track pointing to an energy cluster in a section of the electromagnetic

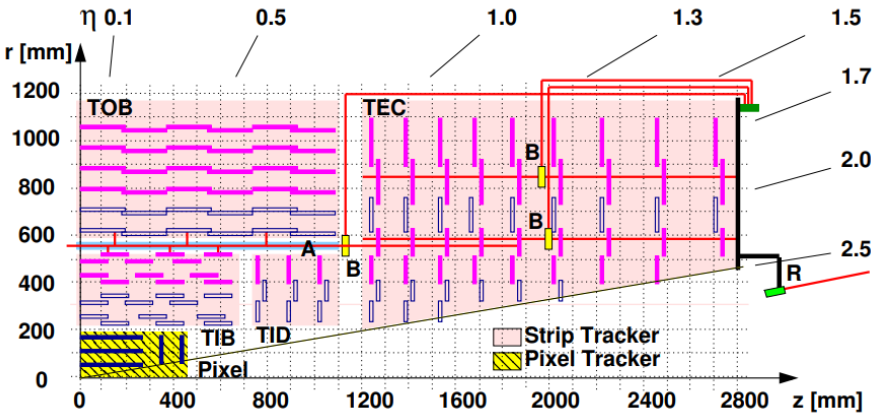

Figure 2.6: Substructures of the CMS silicon tracker: inner barrel (TIB), outer barrel (TOB), inner disks (TID) and endcaps (TEC) are shown for a quarter of the CMS silicon tracker in an rz plane [7]

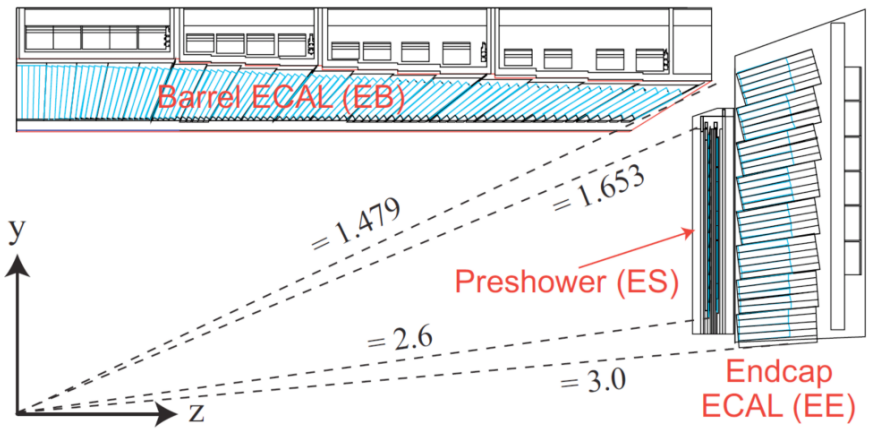

Figure 2.7: Geometric view of one quarter of the CMS electromagnetic calorimeter (ECAL), presenting the arrangement of barrel super-modules, endcaps and the preshower in front [8].

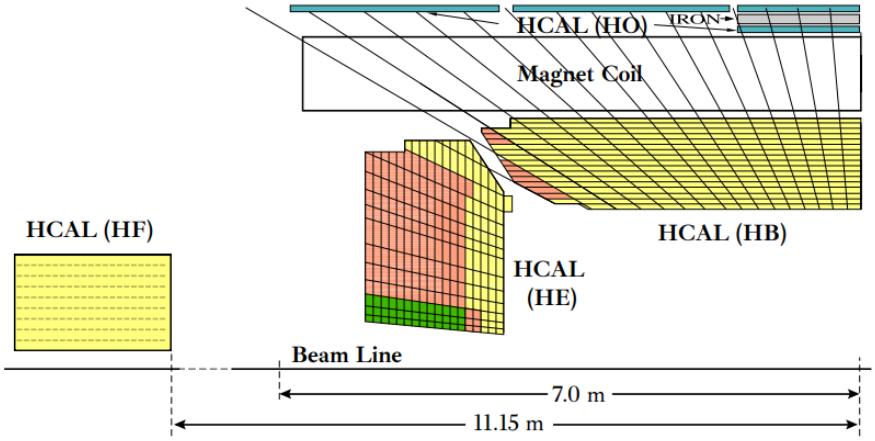

Figure 2.8: Schematic view of the CMS hadron calorimeter (HCAL) in the r-z plane, divided into its subcomponents: HCAL barrel (HB), endcap (HE), outer (HO) and forward (HF) [9].

calorimeter could be associated to an electron or positron candidate. Once these initial blocks are constructed the algorithm proceeds to identify the particles.

2.3.1 Jets

As mentioned in section 1.1.1, quarks and gluons produced in pp collisions hadronize into cones of collimated colorless objects named jets. These jets are reconstructed using a sequential clustering algorithm called anti-kt algorithm [10]. It follows an iterative procedure, which takes the various hadron candidates reconstructed by the PF algorithm and groups them into jets. As shown in Figure 2.9 isolated jets reconstructed with the anti-kt algorithm are associated a characteristic cone-like shape. R is the size of the jet cone in the $\eta - \phi$ plane, which in CMS is chosen to be 0.4.

2.3.2 Missing Transverse Energy

The last step of the PF algorithm involves the measurement of the total transverse energy of the event. In a pp collision the total momenta in the transverse plane must sum up to zero. When this is not verified it means that some energy in the transverse plane is missing in the event. This missing transverse energy could be linked to inefficiencies in the detector or to particles which travelled through the subdetectors without interacting, such as neutrinos or WIMPs. The momentum that these invisible particles are carrying out of the detector can be reconstructed by looking at the full event energy-momentum balance, by computing the imbalance of the momentum measured in the transverse direction. This quantity can be used for reconstructing information about these "invisible" particles, commonly denoted as MET or p_T^{miss}. The vector of missing transverse energy is defined as the negative vector sum of the transverse momenta of all reconstructed PF objects i in the event [1] [66, 67]:

[1] This is known as the PF-MET. There is another MET definition: PileUP per Particle Identification MET or PUPPI-MET, which attempts at reconstructing the MET component originated by the hard scattering process [65].

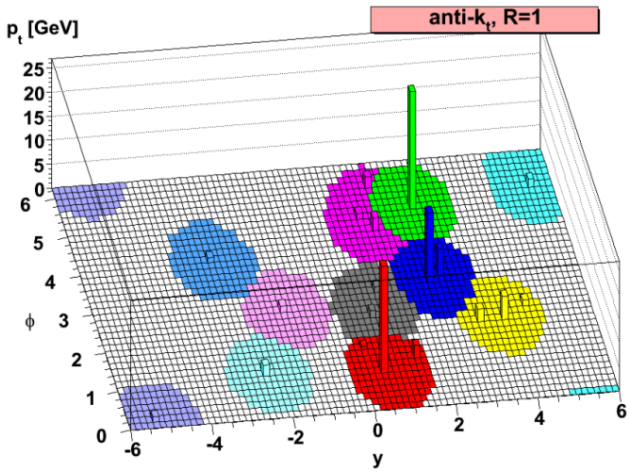

Figure 2.9: Schematic representation of jet clusters reconstructed by the anti-kt algorithm [10]. Each jet cluster is represented by a different color. When relatively isolated, the jets reconstructed with this algorithm are characterized by a cone-like shape.

$$\vec{p}_T^{\,miss} = -\sum_i \vec{p}_T(i) \tag{2.4}$$

2.4 Trigger

As mentioned in 2.1, proton bunches collide once every 25 ns at the LHC interaction points, giving rise to a bunch crossing frequency of 40 MHz. The CMS infrastructure is only able to handle an event rate up to 1 kHz that can be processed by the offline computing systems (largely due to technical restrictions in its maximum data storage capacity and speed), so there is a need to reduce the amount of data that will be stored for further analysis. The main objective of the trigger is to filter events based on their high energy signatures in the detector since the events of primary interest for the experiment are those that originated in collisions with hard parton interactions, which comprise a small proportion of the produced events.

The level-1 trigger (L1) is based on specialized hardware processors that employ information from the muon systems and calorimeters to determine whether to keep the data from a specific bunch crossing, based on a rather basic identification of the detected particles [68]. The L1 trigger lowers the event rate to around 100 kHz after which the high-level trigger (HLT) continues the data processing. The software-based HLT trigger produces an event reconstruction using data from all subdetectors, and chooses whether to maintain an event for the offline analysis. The full set of L1 and HLT selection criteria, including any prescale of the number of selected events, is referred to as a trigger path. The event rate can be lowered to 100-1000 Hz depending on the trigger paths [69].

Chapter 3

Vector Boson Fusion Searches

3.1 Introduction

One of the main features of DM is its small interaction with normal matter. All searches at colliders rely on the production of some visible particle recoiling against the DM, which will subsequently be tagged in the detector as p_T^{miss}. At the LHC, mono-jet analyses have provided a useful strategy to search for DM [15], using simplified models as benchmarks.

In addition, analyses using vector boson fusion (VBF) topology have been used to probe the production of DM particles at the LHC. VBF events are characterized by two interacting vector bosons and two partons from the initial partons resulting in two forward jets plus p_T^{miss}, as illustrated by the Feynman diagram in Fig. 3.1. The VBF topology is characterized by a high invariant mass for the two VBF jets, a geometric location of these two jets in opposite hemispheres of the detector, and a high η separation between the jets [70]. The utility of the VBF topology has been shown in other BSM contexts such as Higgs Portal DM and MSSM [71, 16].

The simplest formulation is a simplified model with a fermionic DM candidate and a scalar mediator or a vector mediator. The mediator couples only to quarks and DM. In the first case to allow the production of the additional mediator in the LHC from proton-proton collision. The second coupling ensures the decay of the mediator into DM particles. The corresponding Lagrangians, following definitions from [2, 72, 73], are given in equations 3.1-3.3 for the scalar mediator case and 3.5-3.7 for the vector mediator case.

$$\mathcal{L}_{DM}^{Y_0} = g_\chi \bar{\chi}\chi Y_0 \tag{3.1}$$

$$\mathcal{L}_{QCD}^{Y_0} = \frac{g_q}{\sqrt{2}} \sum_{i,j} (y_{ij}^u \bar{u}_i u_j + y_{ij}^d \bar{d}_i d_j) Y_0 \tag{3.2}$$

$$\mathcal{L}_{h}^{Y_0} = m_{Y_0} g_{S1} |\phi|^2 Y_0 + g_{S2} |\phi|^2 Y_0^2 \tag{3.3}$$

$$\begin{aligned} \mathcal{L}_{EW}^{Y_0} = \frac{1}{\Lambda} [& g_{h3}^S (D^\mu \phi)^\dagger (D_\mu \phi) \\ & + g_B^S B_{\mu\nu} B^{\mu\nu} + g_W^S W_{\mu\nu}^i W^{i,\mu\nu}] Y_0 \end{aligned} \tag{3.4}$$

$$\mathcal{L}_{DM}^{Y_1} = g_\chi \bar{\chi}\gamma_\mu \chi Y_1^\mu \tag{3.5}$$

$$\mathcal{L}_{QCD}^{Y_1} = \sum_{i,j} (g_{ij}^u \bar{u}_i \gamma_\mu u_j + g_{ij}^d \bar{d}_i \gamma_\mu d_j) Y_1^\mu \tag{3.6}$$

$$\mathcal{L}_{EW}^{Y_1} = g_V \frac{i}{2} (\phi^\dagger (D_\mu \phi) - (D_\mu \phi)^\dagger \phi) Y_1^\mu \tag{3.7}$$

In equations 3.1 and 3.5, g_χ denotes the coupling between the DM particle candidate χ and the mediator Y_0 or Y_1. On the other hand, in equation 3.2, g_q denotes a generic coupling between the new mediator and the up and down type quarks from the SM; while in equation 3.6, g^u_{ij} and g^d_{ij} are the quarks couplings to the vector mediator to up and donw-type quarks correspondingly. Equation 3.3 shows the linear and quadratic couplings of Y_0 with the Higgs scalar field, correspondingly g_{S1} and g_{S2}. In addition, m_{Y_0} corresponds to the mass of the scalar mediator. The interactions between the scalar mediator and the SM bosons are included through effective dimension five operators described in equation 3.4. g^S_{h3} denotes an additional coupling of the scalar mediator with the Higgs field, while g^S_B and g^S_W denote the couplings with SM bosons. The parameter Λ is set to 10 TeV at some large energy scale. Finally, in equation 3.7, g_V denotes the coupling of the vector mediator Y_1 with the SM Higgs scalar field and the electroweak bosons. The ϕ field corresponds to the Higgs doublet. The equation 3.3 gives rise to mixings between the Z boson and the vector mediator. It should be kept in mind that we have taken a simplified version of the Lagrangian for our studies, but in a generic approach pseudoscalar and axial-vector couplings could be also written.

The main processes for DM production through a VBF topology for each of these models are shown in Fig. 3.1.

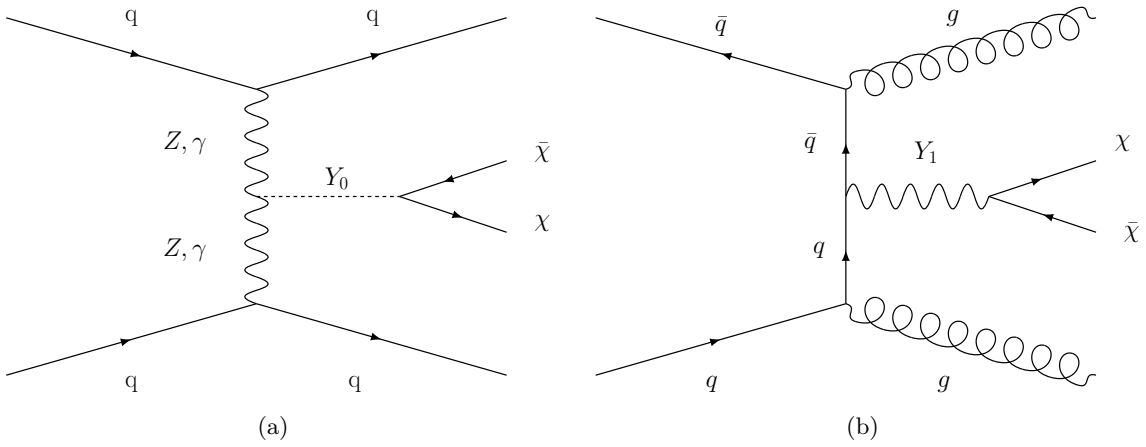

Figure 3.1: Main processes for DM production in a VBF topology: a) Model with a scalar mediator. b) Model with a vector mediator.

The two diagrams share a common structure, but for the scalar mediator case the two final hadronic particles are quarks while in the vector mediator case are gluons. Additionally, in the scalar mediator case the particles mediating the process are vector bosons from the SM and in the vector mediator case are quaks. Therefore, the scalar mediator case is an authentic VBF process very similar to the VBF Higgs production mechanism. This fact allows us to explore the VBF production of DM in a Higgs-like mechanism, but with mediator masses that can be much greater. The vector mediator case is more exotic to DM searches letting us explore new possible scenarios.

Moreover, the simplified models allow us to explore very wide range of mediator masses as well as mediator couplings. These factor are key to our study and will be fully detailed in the next sections.

3.2 Data simulation

3.2.1 Monte Carlo Methods

Simulation is crucial to predict physical interactions among particles as well as those with the detector material. The calculation of the cross-section of fundamental interactions does not provide enough information for a direct comparison with the output of experiments such as CMS. The so-called Monte Carlo (MC) event generators solve this problem by providing possible ways to predict distributions based on theoretical assumptions comparable with experimental observations. These distributions are not only specific for a certain physical process, but also for a particular cross-section. The Monte-Carlo method [74] is based on repeated, random sampling of data in order to achieve a numerical solution for a problem which is not solvable analytically.

To simulate how a physical process happens and how it is measured by a detector, several steps are required. First, the hard-scattering process itself is generated, including incoming and outgoing particles as well as their respective decay products. In this step, the matrix element of the hard process is calculated using the Monte-Carlo method to obtain the properties of the incoming parton. Then, QCD effects of higher orders are taken into account before the hadronization is modeled. Afterwards, a simulated model of the detector is used in order to mimic the reconstruction of the generated particles. In all respective steps, the simulation is tuned to match the observations in data.

Various programs are used to simulate events at the LHC. Pythia8 [75, 76] is used for leading order (LO) event generation. It provides calculations for certain two-body hard-scattering events as well as the hadronization of final-state particles. Processes of higher orders can be estimated based on the parton shower content. MadGraph5 [77], on the other hand, is providing next-to-leading-order (NLO) events. MadGraph calculates the matrix element on tree-level to arbitrary order. To simulate the parton shower and the hadronization, Pythia8 is interfaced by MadGraph. After the particle interactions have been simulated, detector effects have to be taken into account. Thus, the complete CMS detector response is modeled using Delphes [78], including all support structures and detector material. The detector response is emulated by Delphes, using the reconstruction and identification efficiencies of the detector.

3.2.2 Simulated samples

The signal has been simulated from pp collisions at $\sqrt{s} = 13$ TeV in a VBF topology with scalar and vectorial mediators. We used simplified DM models in their *Universal FeynRules Output* (UFO) implementation [79], taken from the FeynRules model database [80, 81, 2]. The signal samples were produced for several combinations of DM and mediator masses points (m_χ, m_Y), ranging from 10 to 1000 GeV and from 100 to 5000 GeV, respectively. The cross sections for fixed mediator mass, fixed couplings and as a function of the DM mass are shown in Figure 3.2.

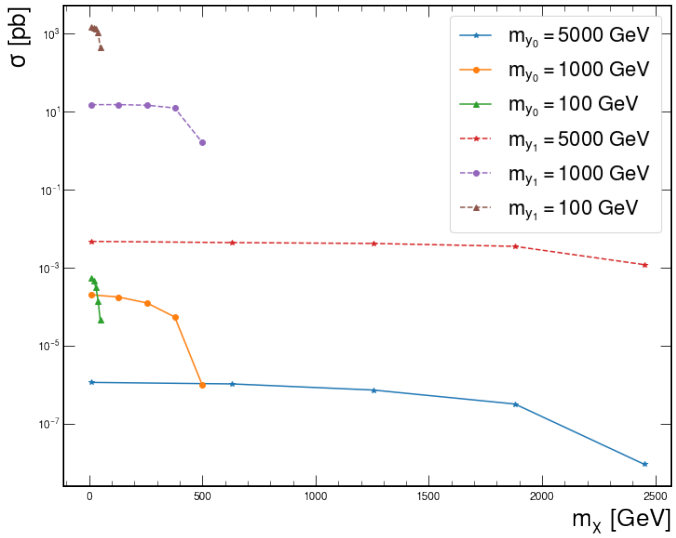

Figure 3.2: Signals cross sections for fixed mediator mass, as described in the legend, setting $g_\chi = 1$ and $g_q = 0.25$ as a function of the DM candidate mass.

Additionally to signal, we also have to consider background processes. There are two categories of backgrounds for DM searches at the LHC. The first is a non-physical background due to a wrong determination of the process states because of uncertainties in the measurements, particles falling into non equipped areas of the detectors, etc. There are also physical backgrounds, in this case, due to the production of neutrinos. The background can be reducible, as in the case of the process where a W boson decays into a charge lepton and a neutrino plus jets in the final state (W+jets). Another background, in this case irreducible, is the Z boson decaying into a pair of neutrinos plus jets (Z+jets). These electroweak bosons produced in association with jets are the primary backgrounds for the analysis. Based on the analysis presented in [82, 83], we have simulated only the Z+jets background, since we assume that W+jets kinematics are similar to Z+jets. Therefore, our background composition will be 70% of Z+jets events and 30% of W+jets events.

The partonic processes for signal and background events have been produced with MadGraph (v3.1.1). The showering and hadronization have been performed by Pythia8, and the detector simulation has been done by Delphes (v3.4.2). Table 3.1 shows the six benchmark models and background used in the analysis.

Table 3.1: Simulated samples for the analysis with their respective number of events and cross sections.

Sample	**Number of events**	**Cross Section** [pb]
$\chi\bar{\chi}jj$ ($m_{Y_0} = 100$, $m_\chi = 10$)	976593	5.31×10^{-3}
$\chi\bar{\chi}jj$ ($m_{Y_0} = 1000$, $m_\chi = 100$)	600000	2.49×10^{-3}
$\chi\bar{\chi}jj$ ($m_{Y_0} = 5000$, $m_\chi = 1000$)	350000	1.36×10^{-5}
$\chi\bar{\chi}jj$ ($m_{Y_1} = 100$, $m_\chi = 10$)	1200000	1.44×10^{3}
$\chi\bar{\chi}jj$ ($m_{Y_1} = 1000$, $m_\chi = 100$)	600000	1.52×10^{1}
$\chi\bar{\chi}jj$ ($m_{Y_1} = 5000$, $m_\chi = 1000$)	550000	4.44×10^{-3}
$Z(\to \nu\nu)$ + Jets	935386	1.24×10^{4}

Table 3.2: Dataset used in the analysis: features, description and variable types.

Feature name	**Feature**	**Description**	**type**
label	Sample label	Sample label: background or signal	str
jet_size	$N(j)$	Number of jets in the event	int
missinget_met	p_T^{miss}	Missing energy transverse momentum in GeV	float
missinget_eta	MET η	Missing energy pseudorapidity	float
missinget_phi	MET ϕ	Missing energy azimuthal angle	float
jet_pt_0	Leading jet p_T	Leading jet transverse momentum in GeV	float
jet_pt_1	Subleading jet p_T	Subleading jet transverse momentum in GeV	float
jet_pt_2	Third jet p_T	Third jet transverse momentum in GeV	float
jet_pt_3	Fourth jet p_T	Fourth jet transverse momentum in GeV	float
jet_eta_0	Leading jet η	Leading jet pseudorapidity	float
jet_eta_1	Subleading jet η	Subleading jet pseudorapidity	float
jet_eta_2	Third jet η	Third jet pseudorapidity	float
jet_eta_3	Fourth jet η	Fourth jet pseudorapidity	float
jet_phi_0	Leading jet ϕ	Leading jet azimuthal angle	float
jet_phi_1	Subleading jet ϕ	Subleading jet azimuthal angle	float
jet_phi_2	Third jet ϕ	Third jet azimuthal angle	float
jet_phi_3	Fourth jet ϕ	Fourth jet azimuthal angle	float
jet_mass_0	Leading jet m	Leading jet mass in GeV	float
jet_mass_1	Subleading jet m	Subleading jet mass in GeV	float
jet_mass_2	Third jet m	Third jet mass in GeV	float
jet_mass_3	Fourth jet m	Fourth jet mass in GeV	float
h	H_T	Total hadronic energy in GeV	float
invariant_mass	m_{jj}	Leading jets invariant mass in GeV	float
delta_phi	$\lvert\Delta\phi_{jj}\rvert$	Leading jets absolute azimuthal angle difference	float
delta_eta	$\lvert\Delta\eta_{jj}\rvert$	Leading jets absolute pseudorapidity difference	float
min_delta_phi_met_jet	min $\lvert\Delta\phi(p_T^{miss},\ j_i)\rvert$	Minimum absolute azimuthal angle difference between MET and jets	float

3.2.3 Dataset

The simulated samples have a tree-like structure, common in the context of high energies physics (HEP), defined by the ROOT format. In this format, the data is very irregular and can be awkward to handle and manage, since its arrays have variable-length dimensions: each entry of the array corresponds to a particle collision event, where each one of these events might have a different number of jets. The Python library Awkward [84] generalizes the array functionalities and provides us with tools for an easy and efficient handling of irregular arrays. Additionally, we use the HEP columnar analysis framework Coffea (Column Object Framework For Effective Analysis) [85] and the Pandas library [86]. With these, we can read the ROOT files from the simulation output and build a regular dataset for the analysis. The dataset contains kinematic features and a sample label, as shown in Table 3.2. Note that we only use the first four jets from each event.

3.3 Event Selection

We have developed an event selection optimizing the significance, defined as $\frac{S}{\sqrt{S+B}}$, using signal events both from scalar and vectorial mediators signals and from $Z(\nu\bar{\nu})$+jets background. We have noted that for both signals considered the optimization had the same results and therefore we end up with one selection regardless of the signal mediator type. The selection begins with very basic criteria mainly driven by well known detector

requirements. This baseline selection is described in Table 3.3.

Table 3.3: Baseline selection.

Criterion	
$N(j)$	> 1
$\eta(j_1) \cdot \eta(j_2)$	< 0
Leading jets p_T	> 30 GeV
Leading jets $\|\eta\|$	< 5
H_T	> 200 GeV
p_T^{miss}	> 50 GeV

The total hadronic energy is defined as $H_T = \sum p_T(j)$ which is the scalar sum of the transverse momentum of all the jets in the event which have a $p_T > 30$ GeV and $|\eta| < 5$. The criterion of $H_T > 200$ GeV is imposed in order to assure a minimum quantity of energy to assure signal events passing the detector trigger. This requirement prevents us to rely on missing transverse momentum for the trigger. We have seen that signal events do not have very high missing transverse momentum (see figure 3.3) and therefore the H_T criterion is very useful to avoid loosing a large amount of signal events by the trigger.

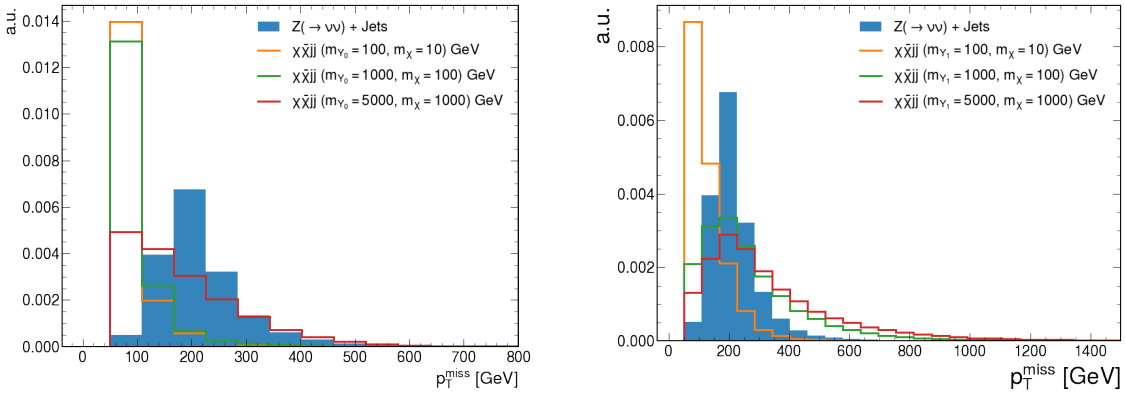

(a) (b)

Figure 3.3: p_T^{miss} after baseline selection for background and signals with (a) a scalar mediator and (b) a vectorial mediator.

For events surviving the baseline selection, we have studied several variables that could potentially increase the signal over background separation. The most discriminant variables are found to be the azimuthal angle difference among the two leading jets $\Delta\phi_{jj}$, their invariant mass m_{jj}, defined as $m_{jj} = \sqrt{2p_T(j_1)p_T(j_2)\left(\cosh\Delta\eta_{jj} - \cos\Delta\phi_{jj}\right)}$, and their pseudorapidity separation $\Delta\eta_{jj}$, shown in 3.4, 3.6, and 3.5, respectively.

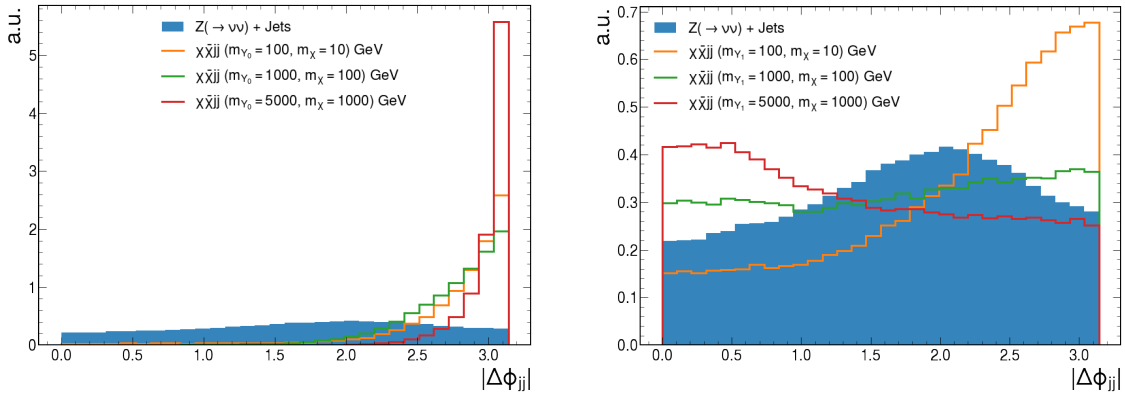

(a) (b)

Figure 3.4: $|\Delta\phi_{jj}|$ after baseline selection for background and signals with (a) a scalar mediator and (b) a vectorial mediator.

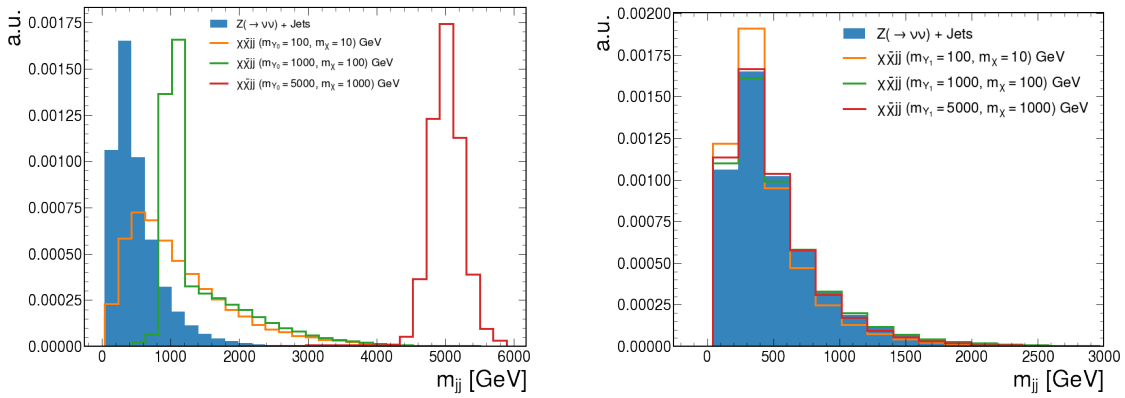

(a) (b)

Figure 3.5: Leading jets invariant mass after baseline selection for background and signals with (a) a scalar mediator and (b) a vectorial mediator.

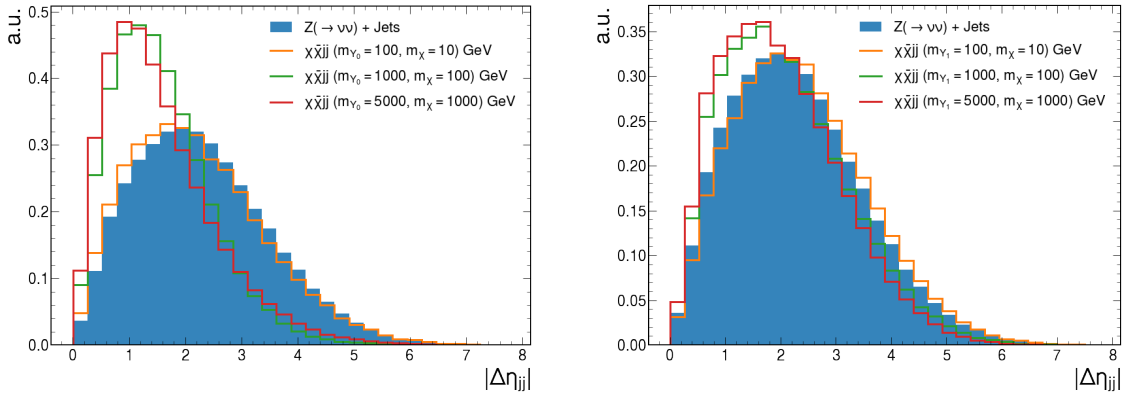

(a) (b)

Figure 3.6: $|\Delta\eta_{jj}|$ after baseline selection for background and signals with (a) a scalar mediator and (b) a vectorial mediator.

The $\Delta\phi_{jj}$ show some dependence on the mediator mass while m_{jj} variable has a homogeneous behavior for different mediator masses. Regarding the classical definition of VBF topology properties the most important finding is the dependence on the mediator masses of the pseudorapidity separation of the two leading jets. In consequence, we start our main selection based on criteria on the azimuthal difference of the leading jets and their invariant mass. From these two first requirements we apply a control criterion intended not for separation of signal with regard to electroweak backgrounds but to actually control the possible contribution from QCD processes to the background. The applied criterion is $\min|\Delta\phi(p_T^{miss}, j_i)| > 0.5$ for the first four leading jets, $i = \{1, 2, 3, 4\}$. This cut ensures having real missing transverse momentum and thus rejecting QCD events [16], [70].

Figure 3.7 show the distribution of signal and background events for $\Delta\eta_{jj}$ after applying the baseline selection and the main selection described above.

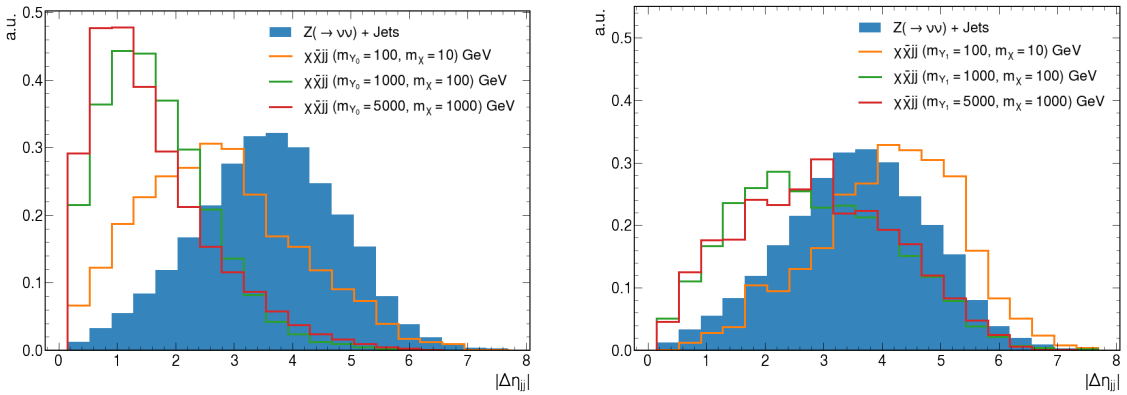

(a) (b)

Figure 3.7: $|\Delta\eta_{jj}|$ after the baseline selection and the three cuts on $|\Delta\phi_{jj}|$, m_{jj}, and $\min|\Delta\phi(p_T^{miss}, j_i)|$, for background and signals with (a) scalar mediator and (b) vectorial mediator.

We see that $\Delta\eta_{jj}$ depends on the mass of the mediator. For high mediator masses,

above 1 TeV, $\Delta\eta_{jj}$ is restricted to low values, while for low mediator masses, below 1 TeV, the $\Delta\eta_{jj}$ is much higher. The most known scenario for VBF topology is for Higgs SM production, which corresponds to our low mass mediator case, from which a high $\Delta\eta_{jj}$ value has been identified as a characteristic feature of VBF, however we see that the pseudorapidity difference for the two VBF jets is not fixed and actually highly anti-correlated to the mediator mass. This finding is also supported by the work done in [83].

In correspondence with this finding, we define two analysis bins optimized to keep events for the two mediator mass scenarios described. Table 3.4 summarizes the event selection

Table 3.4: Event selection. The last line specifies the two bin selections optimized for high and low mediator masses.

Feature	**Value**
m_{jj}	> 1 TeV
$\lvert\Delta\phi_{jj}\rvert$	> 2.3
$\min\lvert\Delta\phi(p_T^{miss}, j_i)\rvert$	< 0.5
$\lvert\Delta\eta_{jj}\rvert$	< 2.5 or > 2.5

Figures 3.8 and 3.9 show the $|\Delta\eta_{jj}|$ distributions for signal events and background after applying all cuts.

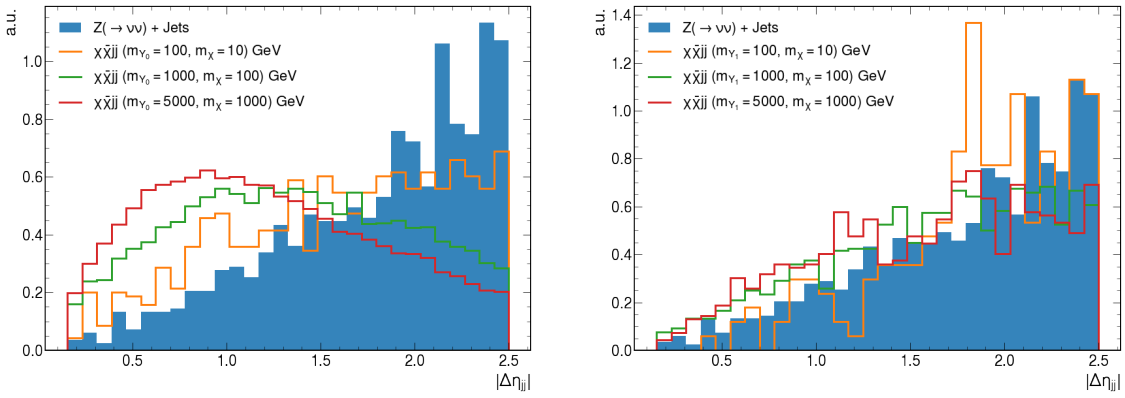

(a) (b)

Figure 3.8: $|\Delta\eta_{jj}|$ after after aplying all other cuts and $|\Delta\eta_{jj}| < 2.5$, for background and signals with (a) scalar mediator and (b) vectorial mediator.

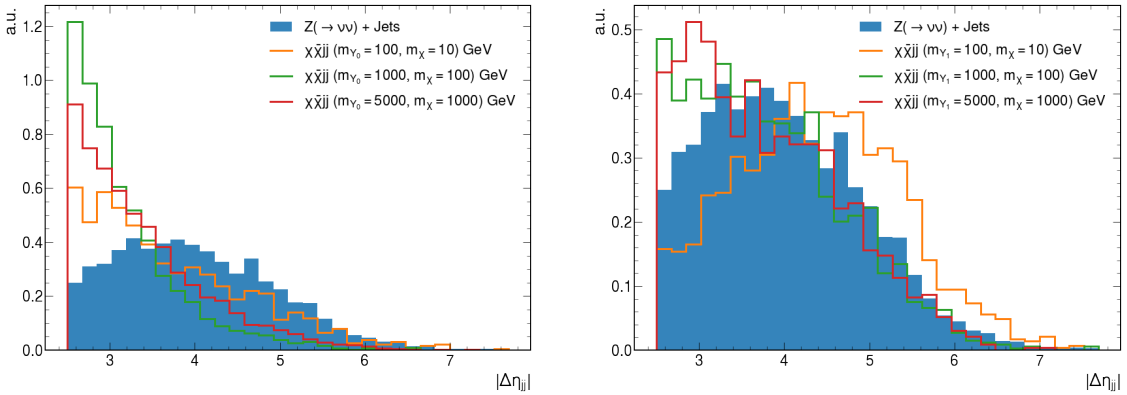

(a) (b)

Figure 3.9: $|\Delta\eta_{jj}|$ after after aplying all other cuts and $|\Delta\eta_{jj}| > 2.5$, for background and signals with (a) scalar mediator and (b) vectorial mediator.

3.4 Results

From the selection developed we establish its reach considering different dark matter and mediator masses. The simplified models approach only depends on four parameters, the dark matter mass, the mediator mass, and the couplings of the mediator to quarks and dark matter. We first establish the significance of the selection for fixed couplings for some benchmark masses. We then analyze the reach of the analysis for fixed masses while variating the couplings.

In Tables 3.5, 3.6 and 3.7 are shown the number of expected events, the significance and cut efficiency as the selection criteria are applied for the three benchmark masses for signal and background for 150 fb^{-1}. The expected number of events are calculated using the cross sections obtained from MadGraph setting both couplings of the mediator to dark matter and quarks $g_\chi = 1$ and $g_q = 0.25$. The cross sections are shown for fixed mediator mass, fixed couplings and as a function of the dark matter mass in Figure 3.2.

Taking into account the dependence of the cross-sections to the couplings and to the mediator and dark matter mass, we have scanned the models parameters in order to identify the exclusion reach of the proposed selections. Figure 3.10 show the excluded areas in the quark coupling-mediator mass plane while having fixed dark matter mass and coupling fixed to 10 GeV and 1.0 respectively. It also shows the exclusion in the quark and dark matter coupling of the mediator, with the mediator mass fixed to 1 TeV and dark matter mass fixed to 10 GeV. The excluded regions are built using a sensitivity $\frac{S}{\sqrt{S+B}}$ of at least 2, and are depicted in the plots as a red line. We have also checked the impact of including 25% of uncertainty in the background yield, but we found only a small difference compared to the limits without uncertainty. In any case, this study shows the feasibility of the proposal, as well as the interest of performing it, a real experimental study might be impacted by many factors that can't be taken into consideration in a phenomenological study. We only reach exclusion for the vectorial mediator scenario. The sensitivity is calculated using the total number of events for each signal sample and backgrounds after selection.

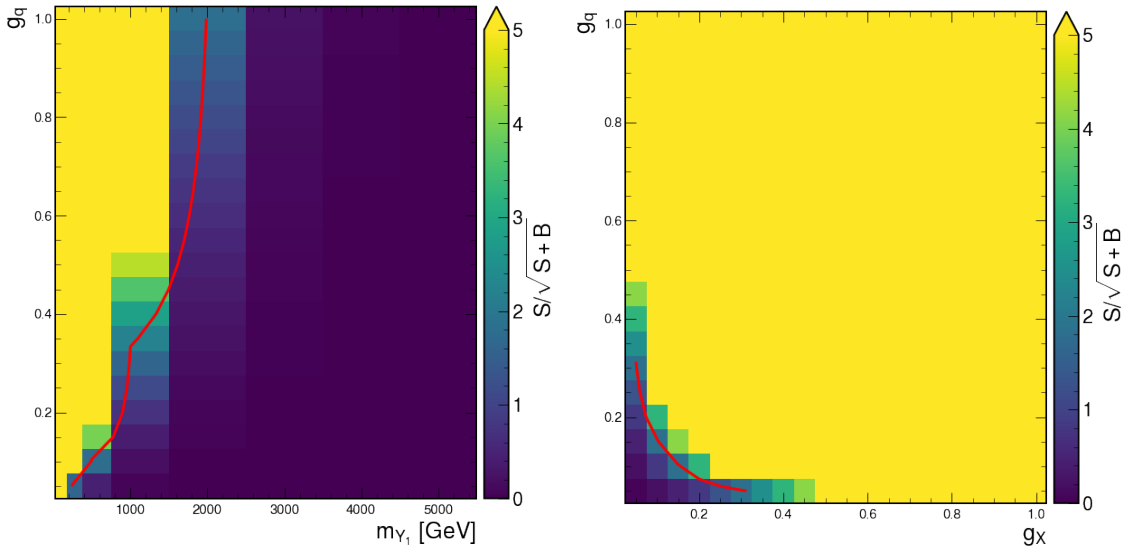

Figure 3.10: Exclusion reach of the selections for [left] g_q-mediator mass where the excluded region is from the red line for greater couplings and smaller mediator masses, and for [right] g_q-g_χ plane with the excluded region from the red line towards higher couplings.

Table 3.5: Events after each selection applied for background and some signals assuming a luminosity of 150fb^{-1}.

	Scalar (m_{Y_0}, m_X) GeV			Vector (m_{Y_1}, m_X) GeV			
Selection	(100,10)	(1000, 100)	(5000, 1000)	(100, 10)	(1000, 100)	(5000,1000)	B
Baseline	3.22e+1	4.43e+5	1.34	6.74e+1	5.26e+5	8.77e-1	4.03e+08
$\lvert\Delta\phi_{jj}\rvert$	2.85e+1	3.95e+5	1.33	3.34e+1	1.57e5	1.94e-1	1.12e+08
m_{jj}	1.41e+1	3.05e+5	1.33	2.64	2.23e+4	2.46e-2	1.64e+07
$\min\lvert\Delta\phi(p_T^{miss}, j_i)\rvert$	1.61	5.69e+4	2.67e-1	1.52	1.32e+4	1.30e-3	1.08e+07
$\lvert\Delta\eta_{jj}\rvert$	7.28e-1, 8.78e-1	4.69e+4, 9.99e+3	2.20e-1, 4.71e-2	1.75e-1, 1.35	5.86e+3, 7.34e+3	5.18e-3, 7.79e-3	2.11e+6, 8.66e+6

Table 3.6: Significance defined as $\frac{S}{\sqrt{S+B}}$ for each signal, including a k-factor (1.2) and a scale factor (1.3) to add the W+jets contribution to the total background, assuming a luminosity of 150fb^{-1}.

	Scalar (m_{Y_0}, m_X) GeV			Vector (m_{Y_1}, m_X) GeV		
Selection	(100, 10)	(1000, 100)	(5000, 1000)	(100, 10)	(1000, 100)	(5000, 1000)
Baseline	2.35e-8	2.74e-4	7.00e-12	1.09e-2	1.79	9.50e-10
$\lvert\Delta\phi_{jj}\rvert$	3.93e-8	4.17e-4	1.31e-11	1.02e-2	1.01	3.98e-10
m_{jj}	5.10e-7	8.41e-4	3.44e-11	2.11e-3	3.76e-1	1.32e-10
$\min\lvert\Delta\phi(p_T^{miss}, j_i)\rvert$	7.16e-9	1.94e-4	8.51e-12	1.51e-3	2.74e-1	8.59e-11
$\lvert\Delta\eta_{jj}\rvert$	7.34e-9, 4.37e-9	3.61e-4, 3.79e-5	1.58e-11, 1.68e-12	3.92e-4, 1.49e-3	2.75e-1, 1.70e-1	7.76e-11, 5.76e-11

Table 3.7: Criteria efficiency for each signal point considered and for background.

	Scalar (m_{Y_0}, m_X) GeV			Vector (m_{Y_1}, m_X) GeV			
Selection	(100,10)	(1000,100)	(5000,1000)	(100,10)	(1000,100)	(5000,1000)	B
Baseline	0.040	0.194	0.658	0.068	0.230	0.273	0.216
$\lvert\Delta\phi_{jj}\rvert$	0.884	0.891	0.991	0.495	0.298	0.221	0.278
m_{jj}	0.495	0.770	0.999	0.078	0.142	0.126	0.145
$\min\lvert\Delta\phi(p_T^{miss}, j_i)\rvert$	0.113	0.186	0.200	0.577	0.591	0.527	0.657
$\lvert\Delta\eta_{jj}\rvert$	0.453, 0.546	0.824, 0.175	0.823, 0.176	0.115, 0.884	0.443, 0.556	0.399, 0.600	0.195, 0.804

Chapter 4

Conclusions and perspectives

From the results shown, we can state that VBF searches for dark matter show a reach up to 2 TeV in the mediator mass and down to 0.2 for the couplings in the vectorial mediator case. These results are compatible with the results achieved by monojet searches [87] and complementary because they impose limits on a different signature, which should be in nature if monojet process is allowed.

In the latest iteration of the monojet DM search done by CMS [88] and ATLAS [89] experiments, the main process considered for DM production is controlled in the simplified models approach by the coupling of the mediator and quarks and the coupling of the mediator to the DM particle. Therefore, the monojet process is controlled by the same parameters for monojet and VBF for the vector mediator, while it is not the case for the scalar mediator. In this sense, the results we obtain for the vector mediator are directly comparable with the monojet results. According to the latest results on the monojet searches, the experiments report results for a benchmark where they have fixed $g_q = 0.25$ and $g_\chi = 1$ and the mediator as the DM are varied. For low DM masses, below 100 GeV, monojet searches reach typically exclusion of the mediator mass up to around 2 TeV. In this work we show that for the same values of the couplings we can only reach up to around 1 TeV. However, as our proposal does not rely strongly on missing momentum it doesn't require specially high DM masses.

We find exclusion for the vector mediator case, however, and due to the small cross-sections, the exclusion is not achieved in the scalar mediator case. This might be improved in other theoretical and experimental scenarios. For example, a coupling of the scalar mediator to the SM W bosons can be added to the model, which would increase the signal production cross-section. On the experimental side, the High Luminosity LHC would give an improved statistical probability of producing signal events. Anyhow, an important finding is that for the simplified models the VBF signature does not differ strongly depending on the spin of the mediator. We should keep in mind that the scalar mediator mass can couple to the W boson, in which case we can increase the production cross-section.

In addition, we could also cover the parameter space of the model in the mediator and dark matter mass plane up to values closer to the diagonal with the dark matter mass equal to half of the mediator mass than the ones already covered by monojet searches. But this would also imply an assumption over the width of the mediator in order to assure stable cross-sections and efficiencies up to the diagonal. In other words, the reach of VBF search is better in the mediator and dark matter mass plane for narrow width mediators (less than 10 GeV) with regard to monojet searches.

We have found that in order to have sensitive VBF searches we might need to optimize

the selections depending on the mediator masses explored due to kinematic differences as the ones we have found for the difference in the pseudorapity of the two VBF jets in the events.

Finally, it would be relevant for the DM community to understand how the combination of the different DM observables constraints the free parameters of simplified models. Since we consider a WIMP scenario we can combine relic density abundance with limits from LHC searches, indirect detection and direct detection. This would be a complimentary work to the one we have developed.

References

[1] Tasneem Saleem. *Development of pixel detector for ATLAS Inner Tracker (ITk) upgrade at HL-LHC and Searching for the Standard Model Higgs boson decay into b-quark pair with ATLAS experiment.* PhD thesis, Université Paris Saclay; Université Paris-Sud; LAL, Laboratoire de l . . . , 2019. (document), 1.1

[2] Jalal Abdallah et al. Simplified Models for Dark Matter Searches at the LHC. *Phys. Dark Univ.*, 9-10:8–23, 2015. (document), 1.2, 3.1, 3.2.2

[3] Julie Haffner. The cern accelerator complex. complexe des acclrateurs du cern, oct, 2013. *URL https://cds. cern. ch/record/1621894. General Photo.* (document), 2.1

[4] CMS Collaboration. Public cms luminosity information, 2021. (document), 2.2

[5] Albert M Sirunyan, Armen Tumasyan, Wolfgang Adam, Ece Asilar, Thomas Bergauer, Johannes Brandstetter, Kadri Özdemir, CMS Collaboration, et al. Particle-flow reconstruction and global event description with the cms detector. *Journal on Instrumentation*, 2017. (document), 2.4, 2.3

[6] Francisco R. Villatoro. Coordinates system used in the cms experiment, 2016. (document), 2.5

[7] CMS collaboration et al. Alignment of the cms silicon tracker during commissioning with cosmic rays. *Journal of Instrumentation*, 5(03):T03009, 2010. (document), 2.2.2, 2.6

[8] S Abdullin, V Abramov, B Acharya, M Adams, N Akchurin, U Akgun, EW Anderson, G Antchev, M Arcidy, S Ayan, et al. Design, performance, and calibration of cms forward calorimeter wedges. *The European Physical Journal C*, 53(1):139–166, 2008. (document), 2.2.3, 2.7

[9] CMS collaboration et al. Performance of cms hadron calorimeter timing and synchronization using test beam, cosmic ray, and lhc beam data. *Journal of Instrumentation*, 5(03):T03013, 2010. (document), 2.2.4, 2.8

[10] Matteo Cacciari, Gavin P Salam, and Gregory Soyez. The anti-kt jet clustering algorithm. *Journal of High Energy Physics*, 2008(04):063, 2008. (document), 2.3.1, 2.9

[11] Kim Griest. The Search for dark matter: WIMPs and MACHOs. *Annals N. Y. Acad. Sci.*, 688:390, 1993. (document)

[12] Vera C Rubin. The rotation of spiral galaxies. *Science*, 220(4604):1339–1344, 1983. (document)

[13] Robert Minchin, Jonathan Davies, Michael Disney, Peter Boyce, Diego Garcia, Christine Jordan, Virginia Kilborn, Robert Lang, Sarah Roberts, Sabina Sabatini, et al. A dark hydrogen cloud in the virgo cluster. *The Astrophysical Journal Letters*, 622(1):L21, 2005. (document)

[14] Viktor Zacek. Dark Matter. In *22nd Lake Louise Winter Institute: Fundamental Interactions*, pages 170–206, 2007. (document)

[15] A. M. Sirunyan et al. Search for new physics in final states with an energetic jet or a hadronically decaying W or Z boson and transverse momentum imbalance at $\sqrt{s} = 13$ TeV. *Phys. Rev. D*, 97(9):092005, 2018. (document), 3.1

[16] Albert M Sirunyan et al. Search for supersymmetry with a compressed mass spectrum in the vector boson fusion topology with 1-lepton and 0-lepton final states in proton-proton collisions at $\sqrt{s} = 13$ TeV. *JHEP*, 08:150, 2019. (document), 3.1, 3.3

[17] Albert M Sirunyan et al. Search for dark matter particles produced in association with a Higgs boson in proton-proton collisions at $\sqrt{s} = 13$ TeV. *JHEP*, 03:025, 2020. (document)

[18] Albert M Sirunyan et al. Search for dark matter produced in association with a leptonically decaying Z boson in proton-proton collisions at $\sqrt{s} = 13$ TeV. *Eur. Phys. J. C*, 81(1):13, 2021. [Erratum: Eur.Phys.J.C 81, 333 (2021)]. (document)

[19] Georges Aad et al. Search for dark matter produced in association with a single top quark in $\sqrt{s} = 13$ TeV pp collisions with the ATLAS detector. *Eur. Phys. J. C*, 81:860, 2021. (document)

[20] Georges Aad et al. Search for new phenomena in events with an energetic jet and missing transverse momentum in pp collisions at $\sqrt{s}$ =13 TeV with the ATLAS detector. *Phys. Rev. D*, 103(11):112006, 2021. (document)

[21] Jalal Abdallah, Adi Ashkenazi, Antonio Boveia, Giorgio Busoni, Andrea De Simone, Caterina Doglioni, Aielet Efrati, Erez Etzion, Johanna Gramling, Thomas Jacques, et al. Simplified models for dark matter and missing energy searches at the lhc. *arXiv preprint arXiv:1409.2893*, 2014. (document)

[22] Sheldon L Glashow. Partial-symmetries of weak interactions. *Nuclear physics*, 22(4):579–588, 1961. 1.1

[23] Abdus Salam. Weak and electromagnetic interactions, inelemen-tary particle physics: Relativistic groups and analyticity, edited by nils svartholm, 1968. 1.1

[24] Steven Weinberg. A model of leptons. *Physical review letters*, 19(21):1264, 1967. 1.1

[25] François Englert and Robert Brout. Broken symmetry and the mass of gauge vector mesons. *Physical review letters*, 13(9):321, 1964. 1.1

[26] Peter W Higgs. Broken symmetries and the masses of gauge bosons. *Physical Review Letters*, 13(16):508, 1964. 1.1, 1.1.2

[27] Gerardus't Hooft. Renormalizable lagrangians for massive yang-mills fields. *Nuclear physics: B*, 35(1):167–188, 1971. 1.1

[28] Gerardus't Hooft. Renormalization of massless yang-mills fields. *Nuclear physics: B*, 33(1):173–199, 1971. 1.1

[29] Oscar W Greenberg. Spin and unitary-spin independence in a paraquark model of baryons and mesons. *Physical Review Letters*, 13(20):598, 1964. 1.1

[30] Moo-Young Han and Yoichiro Nambu. Three-triplet model with double su (3) symmetry. *Physical Review*, 139(4B):B1006, 1965. 1.1

[31] David J Gross and Frank Wilczek. Asymptotically free gauge theories. i. *Physical Review D*, 8(10):3633, 1973. 1.1

[32] David J Gross and Frank Wilczek. Ultraviolet behavior of non-abelian gauge theories. *Physical Review Letters*, 30(26):1343, 1973. 1.1

[33] Arcadi Santamaria. Masses, mixings, yukawa couplings and their symmetries. *Physics Letters B*, 305(1-2):90–97, 1993. 1.1.2

[34] Particle Data Group, PAea Zyla, RM Barnett, J Beringer, O Dahl, DA Dwyer, DE Groom, C-J Lin, KS Lugovsky, E Pianori, et al. Review of particle physics. *Progress of Theoretical and Experimental Physics*, 2020(8):083C01, 2020. 1.1.2

[35] Fritz Zwicky. The redshift of extragalactic nebulae. *Helvetica Physica Acta*, 6:110–127, 1933. 1.2

[36] Marc Kamionkowski and Arthur Kosowsky. The cosmic microwave background and particle physics. *Annual Review of Nuclear and Particle Science*, 49(1):77–123, 1999. 1.2

[37] Saul Perlmutter, Goldhaber Aldering, Gerson Goldhaber, RA Knop, Peter Nugent, Patricia G Castro, Susana Deustua, Sebastien Fabbro, Ariel Goobar, Donald E Groom, et al. Measurements of ω and λ from 42 high-redshift supernovae. *The Astrophysical Journal*, 517(2):565, 1999. 1.2

[38] DH Weinberg, MJ Mortonson, DJ Eisenstein, C Hirata, AG Riess, and E Rozo. Observational probes of cosmic acceleration, phys. rept. 530 (2013) 87–255. *arXiv preprint arXiv:1201.2434*. 1.2

[39] Nabila Aghanim, Yashar Akrami, Mark Ashdown, J Aumont, C Baccigalupi, M Ballardini, AJ Banday, RB Barreiro, N Bartolo, S Basak, et al. Planck 2018 results-vi. cosmological parameters. *Astronomy & Astrophysics*, 641:A6, 2020. 1.2

[40] Laura Baudis. The search for dark matter. *European Review*, 26(1):70–81, 2018. 1.2

[41] Gianfranco Bertone, Dan Hooper, and Joseph Silk. Particle dark matter: Evidence, candidates and constraints. *Physics reports*, 405(5-6):279–390, 2005. 1.2

[42] Dmitry S Gorbunov and Valery A Rubakov. *Introduction to the theory of the early universe: Cosmological perturbations and inflationary theory*. World Scientific, 2011. 1.2

[43] DS Akerib, X Bai, S Bedikian, E Bernard, A Bernstein, A Bolozdynya, A Bradley, D Byram, SB Cahn, C Camp, et al. The large underground xenon (lux) experiment. *Nuclear Instruments and Methods in Physics Research Section A: Accelerators, Spectrometers, Detectors and Associated Equipment*, 704:111–126, 2013. 1.2

[44] P Agnes, IFM Albuquerque, T Alexander, AK Alton, GR Araujo, David M Asner, M Ave, Henning O Back, B Baldin, G Batignani, et al. Low-mass dark matter search with the darkside-50 experiment. *Physical review letters*, 121(8):081307, 2018. 1.2

[45] Elena Aprile, KL Giboni, P Majewski, K Ni, M Yamashita, R Gaitskell, P Sorensen, Luiz DeViveiros, L Baudis, A Bernstein, et al. The xenon dark matter search experiment. *New Astronomy Reviews*, 49(2-6):289–295, 2005. 1.2

[46] Lyndon Evans and Philip Bryant. Lhc machine. *Journal of instrumentation*, 3(08):S08001, 2008. 1.2, 2.1

[47] Csaba Csaki. The Minimal supersymmetric standard model (MSSM). *Mod. Phys. Lett. A*, 11:599, 1996. 1.2.1

[48] Howard E. Haber. The Status of the minimal supersymmetric standard model and beyond. *Nucl. Phys. B Proc. Suppl.*, 62:469–484, 1998. 1.2.1

[49] Ethan M. Dolle and Shufang Su. The Inert Dark Matter. *Phys. Rev. D*, 80:055012, 2009. 1.2.1

[50] A. Goudelis, B. Herrmann, and O. Stål. Dark matter in the Inert Doublet Model after the discovery of a Higgs-like boson at the LHC. *JHEP*, 09:106, 2013. 1.2.1

[51] Howard Georgi. Effective field theory. *Annual review of nuclear and particle science*, 43(1):209–252, 1993. 1.2.1

[52] C. P. Burgess. Introduction to Effective Field Theory. *Ann. Rev. Nucl. Part. Sci.*, 57:329–362, 2007. 1.2.1

[53] CMS Collaboration, S Chatrchyan, G Hmayakyan, V Khachatryan, AM Sirunyan, W Adam, T Bauer, T Bergauer, H Bergauer, M Dragicevic, et al. The cms experiment at the cern lhc. *JInst*, 3:S08004, 2008. 2.1

[54] Kenneth Aamodt, A Abrahantes Quintana, R Achenbach, S Acounis, D Adamová, C Adler, M Aggarwal, F Agnese, G Aglieri Rinella, Z Ahammed, et al. The alice experiment at the cern lhc. *Journal of Instrumentation*, 3(08):S08002, 2008. 2.1

[55] R Achenbach, P Adragna, V Andrei, P Apostologlou, B Åsman, C Ay, BM Barnett, B Bauss, M Bendel, C Bohm, et al. The atlas level-1 calorimeter trigger. *Journal of Instrumentation*, 3(03):P03001, 2008. 2.1

[56] LHCb Collaboration, A Augusto Alves, LM Andrade Filho, AF Barbosa, I Bediaga, G Cernicchiaro, G Guerrer, HP Lima, AA Machado, J Magnin, et al. The lhcb detector at the lhc. *Journal of instrumentation*, 3(08):S08005–S08005, 2008. 2.1

[57] J Knolle. Measuring luminosity and the tżtz production cross section with the cms experiment. 2020. 2.1.1

[58] S Belforte, V Candelise, M Casarsa, A Da Rold, G Della Ricca, G Sorrentino, F Vazzoler, et al. Precision luminosity measurement in proton-proton collisions at sqrt (s)= 13 tev in 2015 and 2016 at cms. 2021. 2.1.1

[59] Olena Karacheban. Luminosity measurement at cms. 2017. 2.1.1

[60] Simon van der Meer. Calibration of the effective beam height in the isr. Technical report, 1968. 2.1.1

[61] A Dominguez et al. Cms technical design report for the pixel detector upgrade. Technical report, Fermi National Accelerator Lab.(FNAL), Batavia, IL (United States), 2012. 2.2.2

[62] Martin Lipinski. The phase-1 upgrade of the cms pixel detector. *Journal of Instrumentation*, 12(07):C07009, 2017. 2.2.2

[63] CMS Collaboration et al. The cms ecal performance with examples. *JINST*, 9:C02008, 2014. 2.2.3

[64] Serguei Chatrchyan, Petar Adžić, Marko Ekmedžić, D Krpić, Predrag Milenović, and Vladimir Reković. Energy calibration and resolution of the cms electromagnetic calorimeter in pp collisions at root s= 7 tev. *Journal of Instrumentation*, 8, 2013. 2.2.3

[65] Daniele Bertolini, Philip Harris, Matthew Low, and Nhan Tran. Pileup per particle identification. *Journal of High Energy Physics*, 2014(10):1–22, 2014. 1

[66] CMS collaboration et al. Missing transverse energy performance of the cms detector. *Journal of Instrumentation*, 6(09):P09001, 2011. 2.3.2

[67] Vardan Khachatryan, Albert M Sirunyan, Armen Tumasyan, Wolfgang Adam, Thomas Bergauer, Marko Dragicevic, Janos Erö, Christian Fabjan, Markus Friedl, Rudolf Fruehwirth, et al. Performance of the cms missing transverse momentum reconstruction in pp data at root s= 8 tev. *Journal of Instrumentation*, pages 1–57, 2015. 2.3.2

[68] GL Bayatian, A Korablev, A Soha, O Sharif, M Chertok, W Mitaroff, F Pauss, V Genchev, M Wensveen, V Lemaitre, et al. Cms physics: Technical design report volume 1: Detector performance and software. Technical report, CMS-TDR-008-1, 2006. 2.4

[69] Vardan Khachatryan, Albert M Sirunyan, Armen Tumasyan, Wolfgang Adam, E Asilar, Thomas Bergauer, Johannes Brandstetter, Erica Brondolin, Marko Dragicevic, Janos Erö, et al. The cms trigger system. *Journal of Instrumentation*, 12(01):P01020–P01020, 2017. 2.4

[70] Albert M Sirunyan et al. Search for invisible decays of a Higgs boson produced through vector boson fusion in proton-proton collisions at $\sqrt{s} = 13$ TeV. *Phys. Lett. B*, 793:520–551, 2019. 3.1, 3.3

[71] Bhaskar Dutta, Guillermo Palacio, Jose D. Ruiz-Alvarez, and Diego Restrepo. Vector Boson Fusion in the Inert Doublet Model. *Phys. Rev. D*, 97(5):055045, 2018. 3.1

[72] Mihailo Backović, Michael Krämer, Fabio Maltoni, Antony Martini, Kentarou Mawatari, and Mathieu Pellen. Higher-order QCD predictions for dark matter production at the LHC in simplified models with s-channel mediators. *Eur. Phys. J. C*, 75(10):482, 2015. 3.1

[73] Matthias Neubert, Jian Wang, and Cen Zhang. Higher-Order QCD Predictions for Dark Matter Production in Mono-Z Searches at the LHC. *JHEP*, 02:082, 2016. 3.1

[74] W Keith Hastings. Monte carlo sampling methods using markov chains and their applications. 1970. 3.2.1

[75] Torbjorn Sjostrand, Stephen Mrenna, and Peter Z. Skands. PYTHIA 6.4 Physics and Manual. *JHEP*, 05:026, 2006. 3.2.1

[76] Torbjörn Sjöstrand, Stefan Ask, Jesper R. Christiansen, Richard Corke, Nishita Desai, Philip Ilten, Stephen Mrenna, Stefan Prestel, Christine O. Rasmussen, and Peter Z. Skands. An introduction to PYTHIA 8.2. *Comput. Phys. Commun.*, 191:159–177, 2015. 3.2.1

[77] J. Alwall, R. Frederix, S. Frixione, V. Hirschi, F. Maltoni, O. Mattelaer, H. S. Shao, T. Stelzer, P. Torrielli, and M. Zaro. The automated computation of tree-level and next-to-leading order differential cross sections, and their matching to parton shower simulations. *JHEP*, 07:079, 2014. 3.2.1

[78] J. de Favereau, C. Delaere, P. Demin, A. Giammanco, V. Lemaître, A. Mertens, and M. Selvaggi. DELPHES 3, A modular framework for fast simulation of a generic collider experiment. *JHEP*, 02:057, 2014. 3.2.1

[79] Celine Degrande, Claude Duhr, Benjamin Fuks, David Grellscheid, Olivier Mattelaer, and Thomas Reiter. UFO - The Universal FeynRules Output. *Comput. Phys. Commun.*, 183:1201–1214, 2012. 3.2.2

[80] Jalal Abdallah et al. Simplified Models for Dark Matter and Missing Energy Searches at the LHC. 9 2014. 3.2.2

[81] Matthew R. Buckley, David Feld, and Dorival Goncalves. Scalar Simplified Models for Dark Matter. *Phys. Rev. D*, 91:015017, 2015. 3.2.2

[82] CMS collaboration et al. Search for dark matter and supersymmetry with a compressed mass spectrum in the vector boson fusion topology in proton-proton collisions at sqrt (s)= 8 tev. *arXiv preprint arXiv:1605.09305*, 2016. 3.2.2

[83] Andrés Flórez, Alfredo Gurrola, Will Johns, Jessica Maruri, Paul Sheldon, Kuver Sinha, and Savanna Rae Starko. Anapole dark matter via vector boson fusion processes at the lhc. *Physical Review D*, 100(1):016017, 2019. 3.2.2, 3.3

[84] Jim Pivarski, Ianna Osborne, Ioana Ifrim, Henry Schreiner, Angus Hollands, Anish Biswas, Pratyush Das, Santam Roy Choudhury, and Nicholas Smith. Awkward Array, 10 2018. 3.2.3

[85] Nicholas Smith, Lindsey Gray, Matteo Cremonesi, Bo Jayatilaka, Oliver Gutsche, Allison Hall, Kevin Pedro, Maria Acosta, Andrew Melo, Stefano Belforte, et al. Coffea columnar object framework for effective analysis. In *EPJ Web of Conferences*, volume 245, page 06012. EDP Sciences, 2020. 3.2.3

[86] The pandas development team. pandas-dev/pandas: Pandas, February 2020. 3.2.3

[87] CMS collaboration et al. Search for new physics in final states with an energetic jet or a hadronically decaying w or z boson and transverse momentum imbalance at $\sqrt{s} = 13$ tev. *arXiv preprint arXiv:1712.02345*, 2017. 4

[88] Albert M Sirunyan, Armen Tumasyan, Wolfgang Adam, E Asilar, Thomas Bergauer, Johannes Brandstetter, Erica Brondolin, Marko Dragicevic, Janos Erö, Martin Flechl, et al. Search for dark matter produced with an energetic jet or a hadronically decaying w or z boson at $\sqrt{s} = 13$ tev. *Journal of High Energy Physics*, 2017(7):1–50, 2017. 4

[89] Georges Aad, Brad Abbott, Dale Charles Abbott, A Abed Abud, Kira Abeling, Deshan Kavishka Abhayasinghe, Syed Haider Abidi, OS AbouZeid, Nadine L Abraham, Halina Abramowicz, et al. Search for new phenomena in events with an energetic jet and missing transverse momentum in p p collisions at s= 13 tev with the atlas detector. *Physical Review D*, 103(11):112006, 2021. 4